



Quantitation of Femtomolar-Level Protein Biomarkers Using a Simple Microbubbling Digital Assay and Bright-Field Smartphone Imaging

Hui Chen, Zhao Li, Lingzhi Zhang, Philippe Sawaya, Jianbo Shi, and Ping Wang*

Abstract: Quantitating ultra-low concentrations of protein biomarkers is critical for early disease diagnosis and treatment. However, most current point-of-care (POC) assays are limited in sensitivity. Herein, we introduce an ultra-sensitive and facile microbubbling assay for the quantification of protein biomarkers with a digital-readout method that requires only a smartphone camera. We used machine learning to develop a smartphone application for automated image analysis to facilitate accurate and robust counting. Using this method, post-prostatectomy surveillance of prostate specific antigen (PSA) can be achieved with a detection limit (LOD) of 2.1 fM (0.060 pg mL^{-1}), and early pregnancy detection using βhCG can be achieved with a of $0.034 \text{ mIU mL}^{-1}$ (2.84 pg mL^{-1}). This work provides the proof-of-principle of the microbubbling assay with a digital readout as an ultra-sensitive technology with minimal requirement for power and accessories, facilitating future POC applications.

Introduction

Point-of-care (POC) protein assays provide clinically actionable quantification of protein biomarkers at the point-of-use, requiring no sample processing or analysis from a remote clinical central laboratory,^[1,2] and meet the increasing demand of patient-centered health care.^[3,4] They connect the testing and the consultation process for patients and therefore avoid multiple visits to healthcare providers, otherwise required by centralized testing.^[3] However, most current POC protein assays, such as the market-dominating lateral-flow assays, are limited in sensitivity and precision.^[5] The beginning of the 21st century witnessed significant advances in pursuit of ultra-high sensitivity protein-biomarker detection in the research settings.^[6–9] In 2010, Rissin et al. reported the single-molecule enzyme-linked immunosorbent assay (digital ELISA), which introduced the digital-assay concept into the field of protein detection.^[8] In digital ELISA, individual protein molecules were directly counted using a discrete, digital fluorescent readout, achieving PCR-like sensitivity for protein detection.

Although sensors in digital assays only need to distinguish between positive and negative signals,^[10] digital ELISA mainly relies on fluorescent labels and requires a sophisticated and nonportable laboratory-based high-resolution fluorescence microscopy system.

Direct visualization as a readout method is more suitable for POC use than fluorescence, since no extra optical system is needed to filter excitation and emission light. Replacing the fluorescent labels in digital ELISA with submillimeter-sized bright-field visible labels (such as microparticles) will pave the way to direct visualization. However, unlike nanosized labels, it is challenging to directly label discrete biomolecules with individual microscope-visible particles. For example, Tekin et al. tried dipole–dipole-assisted interactions and well-controlled microfluidic drag force to label protein molecules with 2.8 μm magnetic beads.^[11] Nam et al. used 30 nm gold nanoparticles to label protein molecules and then used nanoparticle-promoted reduction to increase the size of the gold nanoparticle to amplify the signal.^[7]

Results and Discussion

We aim to facilitate the translation of an ultra-high sensitivity assay to POC clinical use by introducing a new signaling strategy: immobilized-microbubbling, a distinguishable, physical transformation involving quick volume amplification with minimum mass increase. We envision microbubbling as an ideal bridge to connect the invisible nano-world to the visible micro-world. Herein, we present the use of platinum nanoparticle (PtNP)-catalyzed immobilized submillimetre-sized microbubbles to visualize protein molecules. We term this application platinum-nanoparticle-based microbubbling assay, which aims for the ultra-sensitive detection of protein biomarkers with bright-field imaging, using a smartphone, as a new readout strategy for POC use, as shown in Figure 1. In the microbubbling digital assay, target protein molecules are captured by the capture antibodies on paramagnetic microbeads (approximately 2.7 μm), and the bound complexes are labeled with PtNPs. The sandwich complexes are loaded together with hydrogen peroxide solution into an array of square-shaped microwells (14 $\mu\text{m} \times 14 \mu\text{m}$, 7 μm depth, 100 \times 100) on the microbubbling microchip via external magnetic field. Microbubbles form as a result of the accumulation of oxygen, catalyzed by the PtNPs^[12] in the microwells, which can be easily seen using a smartphone camera and a mobile microscope (9x magnification). When the ratio of the number of sandwich complexes to the number of microwells is below 1:1, the percentage of sandwich complexes loaded microwells follows Poisson distribution,^[8]

[*] Dr. H. Chen, Dr. Z. Li, Dr. P. Wang
Department of Pathology and Laboratory Medicine,
University of Pennsylvania, Philadelphia, PA 19104 (USA)
E-mail: Ping.Wang2@pennmedicine.upenn.edu
L. Zhang, P. Sawaya, Dr. J. Shi
Department of Computer and Information Science,
University of Pennsylvania, Philadelphia, PA 19104 (USA)

Supporting information, including the experimental section, and the ORCID identification number(s) for the author(s) of this article can be found under:
<https://doi.org/10.1002/anie.201906856>

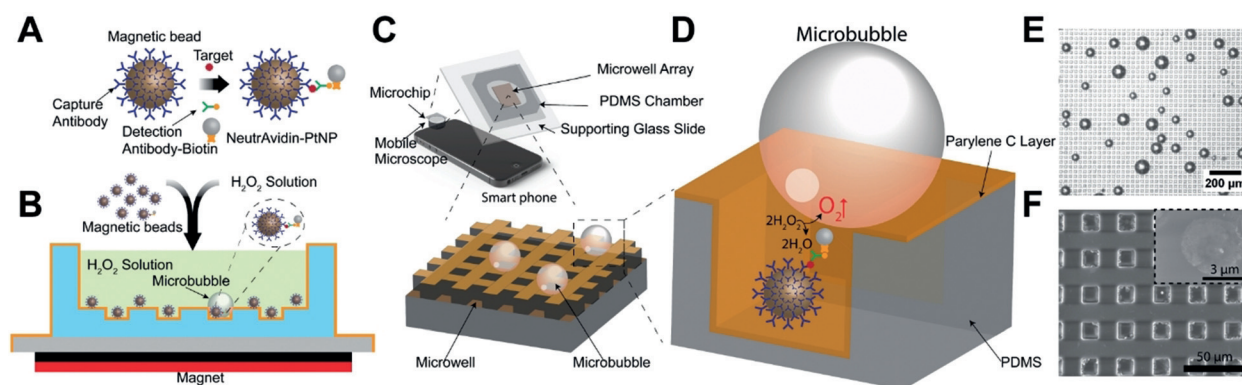


Figure 1. Schematic of platinum nanoparticle based microbubbling assay. A) Magnetic beads functionalized with capture antibodies are used to capture PtNP-labeled target molecules. B) Microbubbling signaling strategy. Magnetic beads with/without PtNPs are loaded together with hydrogen peroxide solution into the microbubbling chip. External magnetic field is then used to settle down the magnetic beads to the bottom of the chip. Distinguishable microbubbles can be observed when magnetic bead/target molecule/PtNP sandwich complexes are present in the microwells in the microbubbling chip. C) Microbubbling microchip with smart phone as readout device. D) Oxygen microbubbles entrapped in the square micro-well array serve as the visible digital signal. Not to scale. E) Microscope image of the microbubbles on the microbubbling chip. Scale bar: 200 μm . F) Scanning electron micrograph of a section of the microbubbling microchip. Scale bar: 50 μm . Inset shows a platinum nanoparticle bound to a paramagnetic bead. Scale bar: 3 μm .

which indicates that the microwells are loaded with a single sandwich complex or none. Therefore, the “yes/no” state of microbubbling digitally represents the “yes/no” state of the existence of a sandwich complex in the microwell. Compared with the analogue signals from PtNPs, such as the ensemble volume or pressure change caused by the PtNPs-catalyzed oxygen generation,^[13,14] the digital (“yes/no” state) signals in the microbubbling assay are less influenced by the environmental temperature and pressure variations. Therefore, the background noise of the microbubbling assay is much lower, resulting in a dramatic increase in sensitivity. Furthermore, like the gold nanoparticles used in lateral-flow immunoassays, the PtNPs used in the microbubbling assay are also stable for long-term storage and transportation.^[15] To ensure the assay readout is precise and user-friendly for POC applications, we have also developed a machine-learning-based automated image analysis smartphone application to count the number of microbubbles under a variety of imaging conditions. To prove the concept, we have used the microbubbling assay to quantitate two model proteins: prostate-specific antigen (PSA) for post-prostatectomy prostate cancer surveillance and β -subunit of human chorionic gonadotropin (βhCG) for early pregnancy detection, as two clinical application examples.

The microbubbling microchip consists of three major parts, as shown in Figure 1C: 1) the sample chamber, 2) the microarray layer, and 3) the supporting glass slide. The size of the microarray is designed to be 3 mm \times 3 mm to fit the field of view of the smartphone imaging system. The microwell is designed in square shape to be easily distinguishable from the round microbubbles. We used standard soft lithography to make the polydimethylsiloxane (PDMS) microwells, which were coated with a 3 μm thick layer of parylene C via physical vapor deposition (PVD) to prevent the diffusion of oxygen into PDMS, as shown in Figure S1 in the Supporting Information. The microbubbling-assay procedure is shown in Figure 1A,B. Magnetic beads, functionalized with capture antibodies, are used to capture target molecules, which are

labeled with PtNPs via detection antibodies. All the magnetic beads with/without PtNPs are loaded into the chamber of the microbubbling chip, together with hydrogen peroxide solution. External magnetic field (by placing a magnet under the microbubbling chip for 1 min) is used to settle all the magnetic beads to the bottom of the microbubbling chip. Microbubbles can be observed in the microwells of the chip, when magnetic bead/target molecule/PtNP sandwich complexes are present in the corresponding microwells. We found that the formation of microbubbles is microwell-dependent. As shown in Figure S2 in the Supporting Information, microbubbles were only found in the microwell area but not in other areas without microwells. We hypothesize that the growth of the microbubbles is facilitated by the rapid local oxygen accumulation in the microwells. To assess the kinetics of the microbubbling process on the microchip, we first used biotinylated bovine serum albumin (bBSA)-coated paramagnetic microbeads to capture NeutrAvidin-functionalized PtNPs, and then loaded the beads together with hydrogen peroxide solution into the microwell array on a microbubbling microchip via an external magnetic field. As shown in Figure 2A and Movie S1 in the Supporting Information (recorded using a conventional microscope, 100X magnification) and Movie S2 in the Supporting Information (recorded at 9X magnification using a smartphone camera and a mobile microscope), the microbubbles formed quickly after the beads were loaded. All the microbubbles became visible under a conventional microscope within 8 min. All the microbubbles originated from the centers of corresponding microwells and kept growing with these microwells as centers, indicating the growth of the microbubbles was powered by the gas-generating reaction catalyzed by the PtNPs trapped in the corresponding microwells. This was further confirmed by the finding that replacing the solution in the microchip with fresh hydrogen peroxide solution resulted in the production of new bubbles in the exact same microwells (Supporting Information, Figure S3). As shown in Figure 2B,C, microbubbles

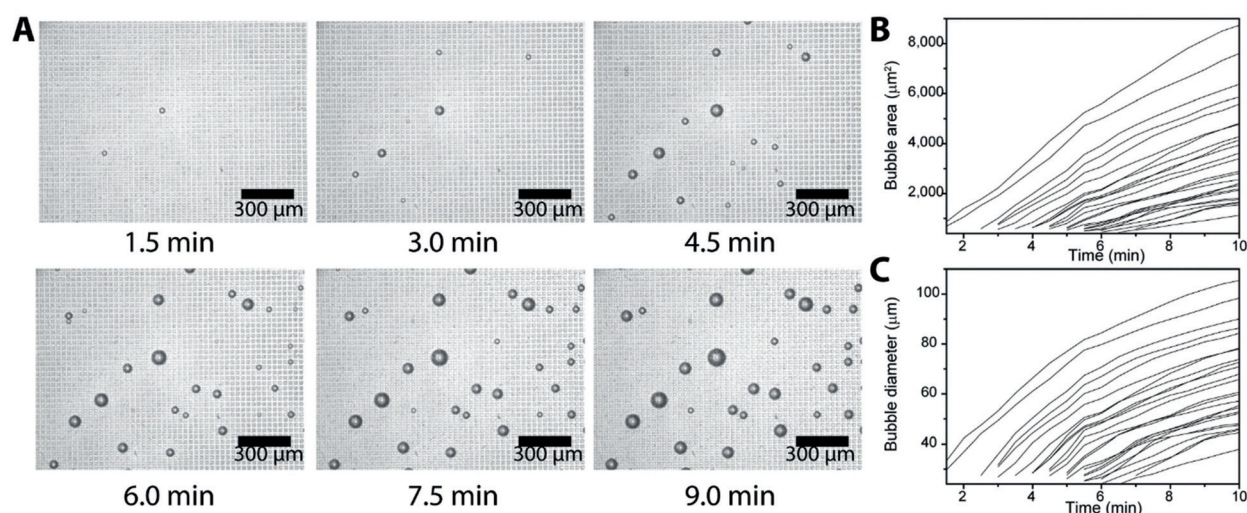


Figure 2. Kinetics of microbubbling. A) Microscope images of the microbubbles growing on a section of the microchip (scale bars: 300 μm). About 25 000 Neutravidin functionalized platinum nanoparticles were incubated with biotinylated bovine serum albumin (bBSA) functionalized paramagnetic beads and loaded onto the microbubbling chip via external magnetic field. Time 0 was set as the point that the magnetic field was applied. Measurements of the microbubble (B) areas and C) diameters as a function of time. Each trace represents the growth of one individual microbubble.

started appearing at different time points, indicating the increase of local oxygen concentrations varied in different microwells. This is possibly due to the variations in number, size, mass transfer, shape, and surface coverage of the PtNPs in these bubble-generating microwells. Ambient temperature does not significantly affect the kinetics of bubble growth, as shown in Figure S4 in the Supporting Information. We hypothesize that the formation of microbubbles in the microbubbling assay is a composite chemical–physical phenomenon dependent on the balance between the local generation and the diffusion (into the bulk of the liquid phase) of oxygen molecules. When the local speed of oxygen generation surpasses the speed of oxygen diffusion into the bulk liquid phase, microbubbles form and grow. This is supported by the finding that microbubbles were only found in microwells where the diffusion of oxygen molecules into the bulk liquid phase was restricted by the walls of microwells. When the temperature increases, both the generation and the diffusion speed of oxygen molecules increase, resulting in a relatively constant overall microbubble-growth speed in the range from 4 °C to 32 °C.

To explore the intrinsic sensitivity of the microbubbling assay, we first optimized the amount of magnetic beads (Supporting Information, Figures S5 and S6) and concentration of hydrogen peroxide solution (Supporting Information, Figure S7). We have optimized the ratio between the number of magnetic beads (approximately 200 000) and the number of microwells (10 000) in the assay to make sure most of the microwells are loaded with magnetic beads in each measurement (Supporting Information, Figure S6). We used bBSA-coated paramagnetic microbeads to capture a range of numbers of NeutrAvidin-functionalized PtNPs, and then loaded the beads together with hydrogen peroxide solution into the microwell arrays on microbubbling microchips via external magnetic field. After 8 minutes, the microbubbles on the microbubbling microchips were imaged using an iPhone 6

plus together with a commercial mobile microscope (9x magnification). As shown in Figure 3, the number of microbubbles correlated linearly with the number of PtNPs, with a limit of detection (LOD) of 894 PtNPs. The LOD was calculated by extrapolating the amount of PtNPs at background plus 3 standard deviations of the background.

Thanks to their unique light-scattering properties and shape, the microbubbles can be easily distinguished in the images by human eye or a conventional image-processing algorithm. But the color and brightness of microbubbles may vary significantly as shown in Figure S8 in the Supporting Information, when images are taken under a variety of illumination conditions, which is typical in POC settings. To increase the robustness and accuracy of the image-processing algorithm for bubble counting, we took advantage of a convolutional neural network (CNN) to identify and count the number of microbubbles in the images. CNN has been utilized in the past several years in vision tasks, such as image recognition, semantic segmentation, and object detection.^[16–18] The main advantage of the CNN architecture is that it can learn expressive feature representation with high-level semantics for specific tasks, and it is robust to poor image quality due to less-than-ideal imaging conditions. We developed a smartphone application for microbubbling detection using the CNN, Figure 4A. After training the algorithm with 493 images (detailed training network and process in the Supporting Information, Figure S8), the application can successfully identify the boundaries of the microarray areas and count the microbubbles in seconds. The application is robust to variations in illumination condition and microbubble size and overlapping cases (Supporting Information, Figure S8). Examples of the smartphone application interfaces are as shown in Figure 4B and Movie S3 in the Supporting Information. As shown in Figure 4C, the microbubble counts of 22 test images using the CNN correlate well with ImageJ-assisted manual counts.

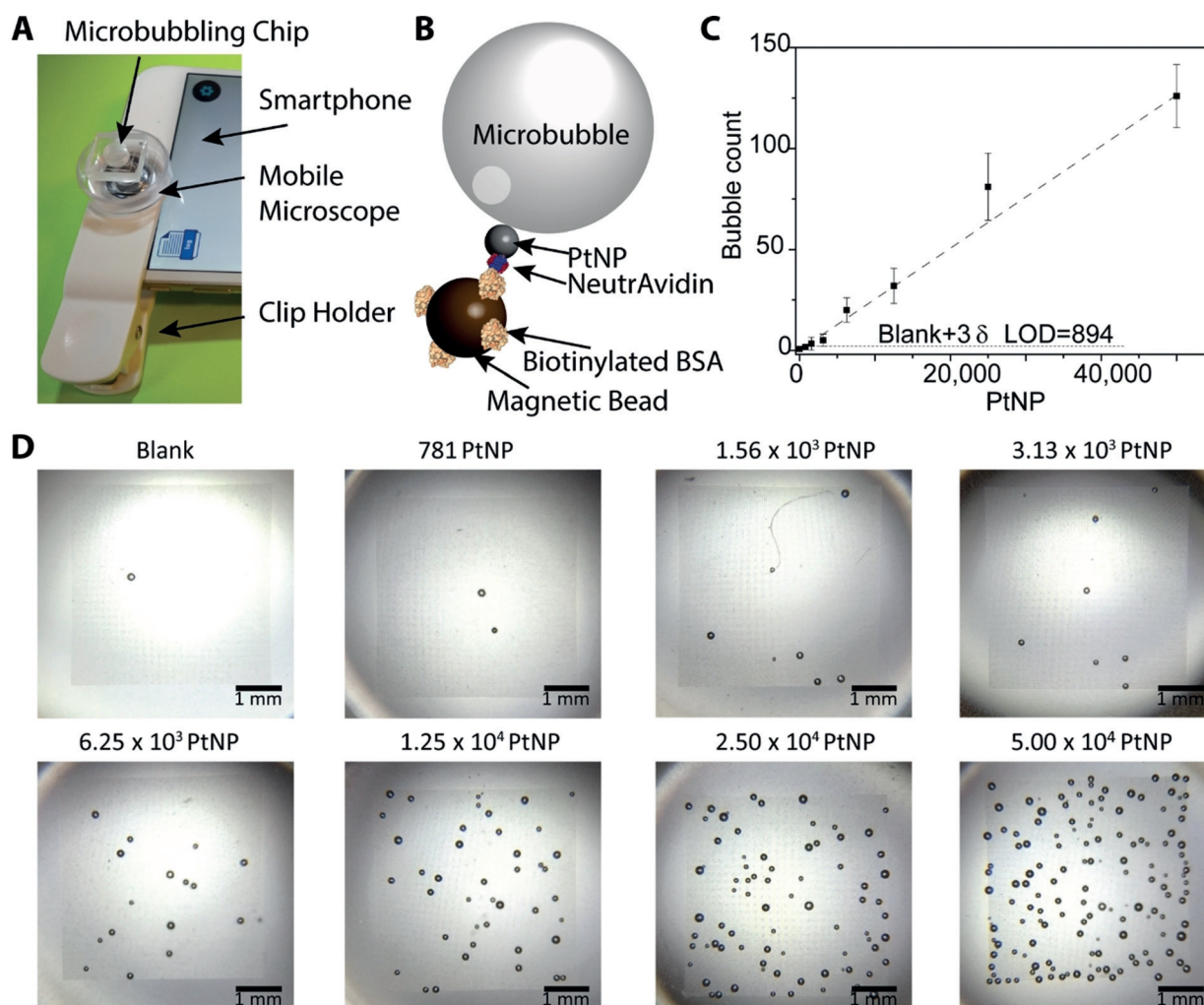


Figure 3. Intrinsic sensitivity assessment of the microbubbling assay. A) Device setup for imaging microbubbles on microbubbling chip with a commercially available mobile microscope (9 \times) and a smartphone. B) Scheme of detecting NeutrAvidin coated PtNP using biotinylated bovine serum albumin (bBSA) functionalized magnetic beads via microbubbling. C) Dose-response curve generated from experiments in B. The number of microbubbles correlates linearly with the amount of NeutrAvidin functionalized PtNPs. Mean \pm standard deviation; $n=3$. LOD = 894 PtNPs. D) Smartphone images of the microbubbles that appeared on the microbubbling microchips (scale bars: 1 mm) with different amounts of PtNPs.

Ultrasensitive PSA assessment in the post-prostatectomy surveillance of prostate cancer patients has utility as a means of risk stratification and counselling of patients on prognosis and treatment decisions.^[19–21] Early detection of recurrence offers the possibility of early salvage therapy given at a lower cancer burden and a wider time window for cure.^[22,23] Postoperative PSA >0.073 ng mL⁻¹ at day 30 significantly increased the risk of biochemical recurrence in the presence of positive surgical margins (PSM) after radical prostatectomy, demonstrating that ultrasensitive PSA detection can aid risk stratification in patients with PSM. Patients not likely to experience biochemical recurrence may be spared from the toxicity of immediate adjuvant radiotherapy.^[24] An ultrasensitive POC PSA-detection device would allow urologists to test patients in their offices during follow-up visits after surgery, or eventually allow a telemedicine approach in which patients monitor themselves at home and transmit the results to urologists. This would shorten the time required to detect recurrence, enable immediate discussion of the result as

preferred by the patients,^[25] and administration of salvage therapy if necessary. Studies have reported salvage radiation therapy given soon after elevated PSA levels are detected substantially reduces the risk of relapse and metastasis.^[20,26] Herein, we developed a microbubbling assay to ultrasensitively quantitate PSA for the post-prostatectomy surveillance of prostate cancer, in which the smartphone plays an integral role of data collection, analysis, and transmission. In this assay, paramagnetic microbeads were functionalized with monoclonal anti-PSA antibodies to capture the PSA molecules. Biotinylated polyclonal antibodies were used to label the captured PSA molecules with NeutrAvidin-functionalized PtNPs at the optimized concentration (Supporting Information, Figure S9). As shown in Figure 5 A,B and Figure S10 in the Supporting Information, the number of microbubbles increased as the concentration of PSA increased, and reached plateau at around 500 microbubbles, at which time the bubble density became so high that adjacent microbubbles started to fuse, thus leading to a saturated signal. The dynamic range can

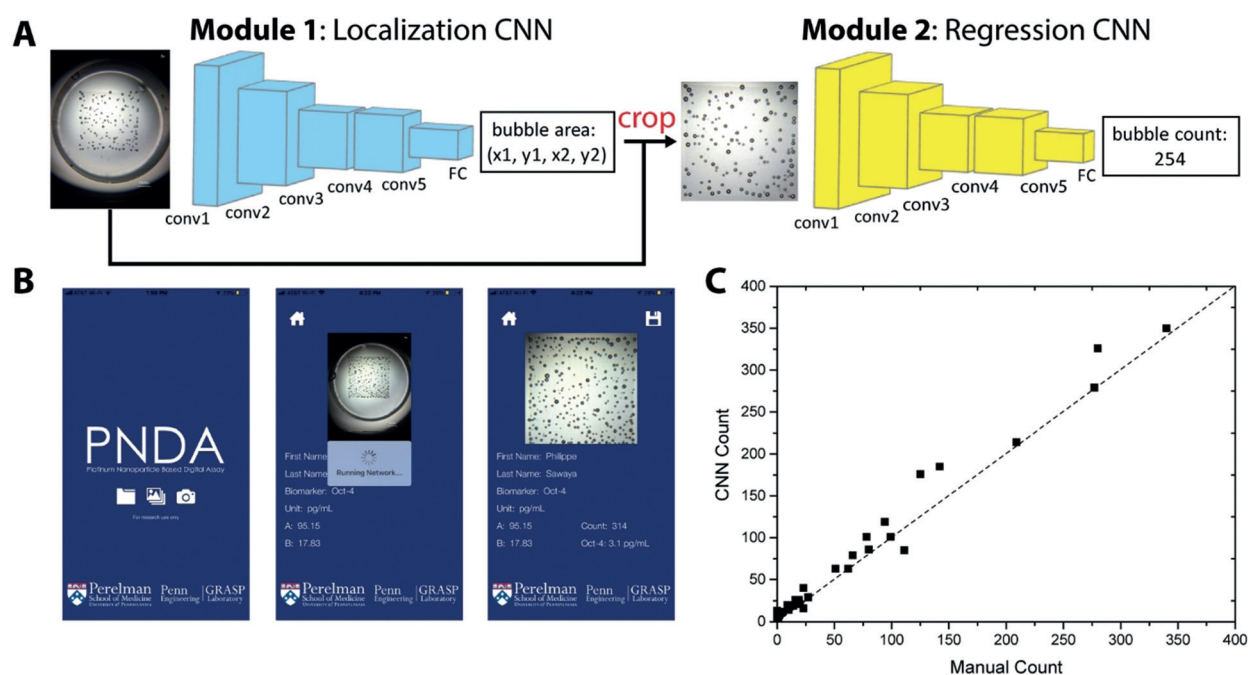


Figure 4. Mobile application via machine learning for counting microbubbles in smartphone images. A) The localization network takes the raw images as input, and outputs the location of the microwell array region. The cropped images are fed into the regression network that outputs the bubble counts. B) User interface of the mobile application. C) The readouts via the CNN approach correlate well with ImageJ-assisted manual approach.

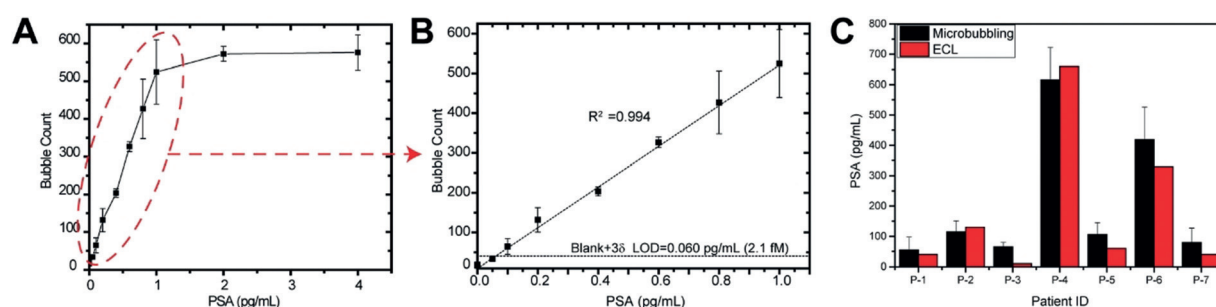


Figure 5. Ultra-sensitive quantitation of prostate specific antigen (PSA) with microbubbling assay for prostate cancer post-prostatectomy surveillance. Anti-PSA monoclonal antibody functionalized paramagnetic beads were used to capture PSA molecules, which were further labeled with the NeutrAvidin functionalized PtNPs via biotinylated anti-PSA polyclonal antibodies. A) Dose-response curve of microbubbling PSA assay. B) In the dynamic range, the number of microbubbles correlates linearly with the concentration of PSA. Mean \pm standard deviation; $n = 4$. $\text{LOD} = 0.060 \text{ pg mL}^{-1}$ (2.1 fM). C) Validation of the microbubbling assay for ultra-sensitive PSA quantitation using patient serum samples. Comparison of PSA results obtained using microbubbling assay with a central clinical laboratory electrochemiluminescence (ECL) assay (Roche Elecsys Cobas Total PSA assay) Mean \pm standard deviation for microbubbling results; $n = 3$.

be expanded by increasing the area or number of the microwell array on the chip. Within the dynamic range ($0.060\text{--}1 \text{ pg mL}^{-1}$), the number of microbubbles correlated linearly with the concentration of PSA, with a limit of detection (LOD) of 2.1 fM (0.060 pg mL^{-1}) PSA. The LOD was calculated by extrapolating the PSA concentration at background plus 3 standard deviations of the background. Compared with the current central clinical laboratory electrochemiluminescence (ECL) assay (Roche Elecsys Cobas Total PSA assay, lower reportable limit 0.01 ng mL^{-1}), the microbubbling assay is 167-times more sensitive. At the current stage, an average coefficient of variation (CV) of 16.5% has been achieved for the detection of PSA with the micro-

bubbling assay, as shown in Table S1 in the Supporting Information. The CV of the microbubbling assay can be further decreased by integrating the platform with automated microfluidic sample preparation, reaction mixing, and washing. To validate the performance of the microbubbling assay in PSA quantitation, we blind-tested 13 prostate cancer patients' serum samples with various PSA concentrations. As shown in Figure 5 C, the microbubbling results correlated well with the central clinical laboratory electrochemiluminescence (ECL) results. In 6 samples with PSA levels undetectable with the ECL assay, the accuracy of the microbubbling results was validated against the Simoa research assay, as shown in Figure S11 in the Supporting Information.

To assess the versatility of the microbubbling assay, we also developed an assay for β hCG, a biomarker for pregnancy. High sensitivity β hCG detection in the POC setting is key to the quick early pregnancy detection, which is useful for pregnancy screening before diagnostic radiography procedures in the emergency department,^[27] and care planning in the home setting. However, the sensitivity and accuracy of most POC β hCG tests are not as good as their central laboratory counterparts, and many are insufficient to detect very early pregnancy.^[28,29] In our microbubbling assay, as shown in Figure S12 in the Supporting Information, the number of microbubbles correlated linearly with the concentration of β hCG, with an LOD of $0.034 \text{ mIU mL}^{-1}$ or 2.84 pg mL^{-1} (background plus 3 standard deviations), with sensitivity significantly higher than current central laboratory (for example, LOD: 0.5 mIU mL^{-1} or 42 pg mL^{-1} for Beckman Coulter chemiluminescence immunoassay (CLIA)) or POC assays (for example, LOD: 5 mIU mL^{-1} or 0.4 ng mL^{-1} for Abbott i-STAT Total β -hCG Test).^[30]

Conclusion

In summary, we have developed a novel ultra-sensitive microbubbling assay with a digital readout method to address the clinical POC need for high-sensitivity protein quantitation. We have demonstrated for the first time that immobilized-microbubbling can be used as a simple and fast digital assay signaling strategy to bridge the invisible nano-world with the visible micro-world. Compared with the ensemble volume or pressure analogue signals of PtNP labels, the microbubbling assay uses a “yes/no” digital signal that is less influenced by variations of environmental temperature and pressure, leading to lower background noises and higher sensitivity.

We envision multiple possibilities to further develop this novel technology platform, based on this proof-of-principle study. The microbubbling assay may be adapted to central laboratory instruments with high quality imaging capabilities for either research or diagnostic purposes. As demonstrated here, this technology also has potential to be further developed for POC diagnostic use, as the microbubbles can be easily imaged with a smartphone and a mobile microscope. We have developed an automated-image-analysis smartphone application using machine learning to make assay readout more user-friendly, robust, and free of potential user bias. At the current stage, multiple hands-on steps are still needed to carry out the incubation and washing steps in microbubbling assays. Further integration with automated systems, such as autonomous capillary microfluidic systems^[31] disk-like microfluidic systems,^[32] and programmable electro-wetting-based droplet-mixing systems,^[33] would simplify the microbubbling assay, making it ready for POC applications. Once integrated, the ultra-sensitive microbubbling assay is a platform that has wide applicability beyond the two model protein biomarkers tested here.

Acknowledgements

This work was performed in part at the Singh Center for Nanotechnology at the University of Pennsylvania, a member of the National Nanotechnology Coordinated Infrastructure (NNCI) network.

Conflict of interest

The authors declare no conflict of interest.

Keywords: biosensors · digital assay · platinum nanoparticles · protein detection · smartphone

How to cite: *Angew. Chem. Int. Ed.* **2019**, *58*, 13922–13928
Angew. Chem. **2019**, *131*, 14060–14066

- [1] B. M. Cummins, F. S. Ligler, G. M. Walker, *Biotechnol. Adv.* **2016**, *34*, 161–176.
- [2] H. Chen, K. Liu, Z. Li, P. Wang, *Clin. Chim. Acta* **2019**, *493*, 138–147.
- [3] A. St John, C. P. Price, *Clin. Biochem. Rev.* **2014**, *35*, 155–167.
- [4] P. Wang, L. J. Kricka, *Clin. Chem.* **2018**, *64*, 1439–1452.
- [5] C. Gaydos, J. Hardick, *Expert Rev. Anti-Infect. Ther.* **2014**, *12*, 657–672.
- [6] S. Fredriksson, M. Gullberg, J. Jarvius, C. Olsson, K. Pietras, S. M. Gústafsdóttir, A. Östman, U. Landegren, *Nat. Biotechnol.* **2002**, *20*, 473.
- [7] J. M. Nam, C. S. Thaxton, C. A. Mirkin, *Science* **2003**, *301*, 1884–1886.
- [8] D. M. Rissin, C. W. Kan, T. G. Campbell, S. C. Howes, D. R. Fournier, L. Song, T. Piech, P. P. Patel, L. Chang, A. J. Rivnak, E. P. Ferrell, J. D. Randall, G. K. Provuncher, D. R. Walt, D. C. Duffy, *Nat. Biotechnol.* **2010**, *28*, 595–599.
- [9] H. Chen, M. Crum, D. Chavan, B. Vu, K. Kourentzi, R. C. Willson, *ACS Appl. Mater. Interfaces* **2018**, *10*, 31845–31849.
- [10] A. S. Basu, *SLAS Technol.* **2017**, *22*, 369–386.
- [11] H. C. Tekin, M. Cornaglia, M. A. Gijs, *Lab Chip* **2013**, *13*, 1053–1059.
- [12] W. F. Paxton, K. C. Kistler, C. C. Olmeda, A. Sen, S. K. St Angelo, Y. Cao, T. E. Mallouk, P. E. Lammert, V. H. Crespi, *J. Am. Chem. Soc.* **2004**, *126*, 13424–13431.
- [13] Z. Zhu, Z. Guan, D. Liu, S. Jia, J. Li, Z. Lei, S. Lin, T. Ji, Z. Tian, C. J. Yang, *Angew. Chem. Int. Ed.* **2015**, *54*, 10448–10453; *Angew. Chem.* **2015**, *127*, 10594–10599.
- [14] Y. Song, Y. Zhang, P. E. Bernard, J. M. Reuben, N. T. Ueno, R. B. Arlinghaus, Y. Zu, L. Qin, *Nat. Commun.* **2012**, *3*, 1283.
- [15] Y. Song, X. Xia, X. Wu, P. Wang, L. Qin, *Angew. Chem. Int. Ed.* **2014**, *53*, 12451–12455; *Angew. Chem.* **2014**, *126*, 12659–12663.
- [16] A. Krizhevsky, I. Sutskever, G. E. Hinton, *Commun. Acm* **2017**, *60*, 84–90.
- [17] E. Shelhamer, J. Long, T. Darrell, *IEEE Trans. Pattern Anal.* **2017**, *39*, 640–651.
- [18] K. He, G. Gkioxari, P. Dollár, R. Girshick, *IEEE International Conference on Computer Vision (ICCV)* **2017**, 2980–2988.
- [19] T. D. Laajala, H. Seikkula, F. Seyednasrollah, T. Mirtti, P. J. Bostrom, L. L. Elo, *Sci. Rep.* **2016**, *6*, 36161.
- [20] D. Tilki, S. I. Kim, B. Hu, M. A. Dall’Era, C. P. Evans, *J. Urol.* **2015**, *193*, 1525–1531.
- [21] L. J. Sokoll, Z. Zhang, D. W. Chan, A. C. Reese, T. J. Bivalacqua, A. W. Partin, P. C. Walsh, *J. Urol.* **2016**, *195*, 330–336.

- [22] A. J. Stephenson, P. T. Scardino, M. W. Kattan, T. M. Pisansky, K. M. Slawin, E. A. Klein, M. S. Anscher, J. M. Michalski, H. M. Sandler, D. W. Lin, J. D. Forman, M. J. Zelefsky, L. L. Kestin, C. G. Roehrborn, C. N. Catton, T. L. DeWeese, S. L. Liauw, R. K. Valicenti, D. A. Kuban, A. Pollack, *J. Clin. Oncol.* **2007**, *25*, 2035–2041.
- [23] S. Shen, H. Lepor, R. Yaffee, S. S. Taneja, *J. Urol.* **2005**, *173*, 777–780.
- [24] S. Vesely, L. Jarolim, K. Duskova, M. Schmidt, P. Dusek, M. Babjuk, *BMC Urol.* **2014**, *14*, 79.
- [25] S. Wilkinson, K. Warren, A. Ramsden, A. Matthews, G. Chodak, *Urology* **2008**, *71*, 567–572.
- [26] R. D. Tendulkar, S. Agrawal, T. Gao, J. A. Efstathiou, T. M. Pisansky, J. M. Michalski, B. F. Koontz, D. A. Hamstra, F. Y. Feng, S. L. Liauw, M. C. Abramowitz, A. Pollack, M. S. Anscher, D. Moghanaki, R. B. Den, K. L. Stephans, A. L. Zietman, W. R. Lee, M. W. Kattan, A. J. Stephenson, *J. Clin. Oncol.* **2016**, *34*, 3648–3654.
- [27] A. I. Abushouk, M. Sanei Taheri, P. Pooransari, S. Mirbaha, A. Rouhipour, A. Baratloo, *Emerg (Tehran)* **2017**, *5*, e60–e60.
- [28] D. N. Greene, R. L. Schmidt, S. M. Kamer, D. G. Grenache, C. Hoke, T. S. Lorey, *Clin. Chim. Acta* **2013**, *415*, 317–321.
- [29] C. Gnoth, S. Johnson, *Geburtshilfe Frauenheilkd.* **2014**, *74*, 661–669.
- [30] C. Y. Chen, Y. M. Hwu, C. P. Chen, C. C. Chang, *Int. J. Nanomed.* **2015**, *10*, 2475–2483.
- [31] R. Safaviéh, D. Juncker, *Lab Chip* **2013**, *13*, 4180–4189.
- [32] J. Gilmore, M. Islam, R. Martinez-Duarte, *Micromachines* **2016**, *7*, 52.
- [33] J. Mok, M. N. Mindrinos, R. W. Davis, M. Javanmard, *Proc. Natl. Acad. Sci. USA* **2014**, *111*, 2110–2115.

Manuscript received: June 2, 2019

Revised manuscript received: July 15, 2019

Accepted manuscript online: July 25, 2019

Version of record online: August 21, 2019